4. Evidence for Amazonian highly viscous lavas in the southern highlands on Mars

Petr Brož[1,2], Ernst Hauber[3], Thomas Platz[4,5] and Matt Balme[5,6]

[1]Institute of Geophysics ASCR, v.v.i., Prague, Czech Republic

[2]Institute of Petrology and Structural Geology, Faculty of Science, Charles University, Prague, Czech Republic

[3]Institute of Planetary Research, DLR, Berlin, Germany

[4]Institute of Geological Sciences, Freie Universität Berlin, Berlin, Germany

[5]Planetary Science Institute, United States

[6]CEPSAR, Open University, Milton Keynes, United Kingdom

Status: Published in Earth and Planetary Science Letters 415,

doi: 10.1016/j.epsl.2015.01.033.

4.0. Abstract

We have identified small-scale volcanic edifices, two cones and three domes with associated flows, within Terra Sirenum, a region situated in the martian southern highlands. Based on thermal, morphological, and morphometrical properties, and the determination of absolute model ages, we conclude that these features were formed by volcanic activity of viscous lavas in the mid-Amazonian epoch, relatively recently in martian history. If our hypothesis is correct, this small volcanic field represents rare evidence of young volcanic activity in the martian highlands in which martian equivalents of terrestrial lava domes and coulées might be present. On Earth, such landforms are usually formed by highly viscous evolved lavas, i.e., andesitic to rhyolitic, for which observational evidence is sparse on Mars. Hence, this field might be one of only a few where martian evolved lavas might be investigated in detail.

4.1. Introduction and background

Volcanism was globally widespread on Mars in the early history of the planet, but became focused with ongoing evolution on two main volcanic provinces in the Tharsis and Elysium regions (Werner, 2009; Robbins et al., 2011; Platz and Michael, 2011; Xiao et al., 2012; Grott et al., 2013). Except for the widespread Hesperian ridged plains (Greeley and Spudis, 1981), and some isolated centres (e.g., Tyrrhenus and Hadriacus Montes (Williams et al., 2009; Robbins et al., 2011), evidence for post-Noachian (<3.7 Ga) volcanism, and in particular for individual volcanic edifices is rare in the martian highlands. It is generally thought that highland volcanism occurred early in Mars' history and stopped not later than ~1 Gyr after planet formation (Williams et al., 2009; Xiao et al., 2012).

The youngest volcanic activity in the Tharsis and Elysium volcanic provinces is characterized by the effusion of low-viscosity basaltic lavas (Vaucher et al., 2009a; Hauber et al., 2011; Platz and Michael, 2011). It was long thought that more evolved (i.e., andesitic to rhyolitic) magma compositions are rare on Mars (Bandfield et al., 2004; Christensen et al., 2005), in contrast to Earth, where these lavas are common (Rogers and Hawkesworth, 2000). More recently, however, based on orbital spectroscopic observations and rover-based in situ measurements, several studies indicate that evolved magmas may have been generated on Mars (Skok et al., 2010; Wray et al., 2013; Stolper et al., 2013; Meslin et al., 2013, Sautter et al., 2014), but there are only few direct observations of kilometer-scale edifices that may be composed of evolved magmas (Rampey et al., 2007, Skok et al., 2010).

On Earth, highly viscous and evolved lavas can produce specific types of small-scale volcanic landforms such as magmatic cryptodomes or extrusive lava domes that are (qualitatively) diagnostic of rheology, and from which composition might be inferred (Fink and Griffiths, 1998). Because of their specific morphology and morphometry, these edifices may be recognized by remote sensing techniques (e.g., Rampey et al., 2007;

Neish et al., 2008). The most promising martian edifices are individual hills in the western Arcadia region which may represent possible crypto- or lava domes (Rampey et al., 2007). Conversely, their spectral absorption characteristics are consistent with the presence of olivine and high-Ca pyroxene, commonly augite, suggesting a basaltic composition, but the possibility that these domes might be more silica-rich (basaltic-andesitic or andesite in composition) was not definitely ruled out (Farrand et al., 2011).

In this study we focus on two cones with associated flow apron features, and three domical structures surrounded by flows, which are all located in the southern highlands. They might represent rare evidences of martian equivalents for terrestrial lava domes and coulées caused by highly viscous (i.e., andesitic to rhyolitic) lavas.

4.2. Data and methods

We used data sets acquired by several cameras on various orbital platforms: Context Camera (CTX; 5–6 m/pixel; Malin et al., 2007), High Resolution Stereo Camera (HRSC; 10-20 m/pixel; Jaumann et al., 2007), High Resolution Imaging Science Experiment (HiRISE; ~30 cm/pixel, McEwen et al., 2007) and THEMIS-IR (day and night; ~100 m/pixel; Christensen et al., 2004). CTX data were processed using the USGS Astrogeology image processing software 'ISIS 3' (Integrated System for Imagers and Spectrometers) and HRSC images using VICAR (Video Imaging Communication And Retrieval) software.

Topographic information was derived from Mars Orbiter Laser Altimeter (MOLA; Zuber et al., 1992; Smith et al., 2001) gridded Digital Elevation Models (DEMs) with 128 pixel/degree resolution (~463 m/pixel) for regional context, and from HRSC DEMs for local scales. HRSC DEMs are interpolated from 3D points with an average intersection error of 12.6 m and most have a regular grid spacing of 50 to 100 m (Scholten et al., 2005;

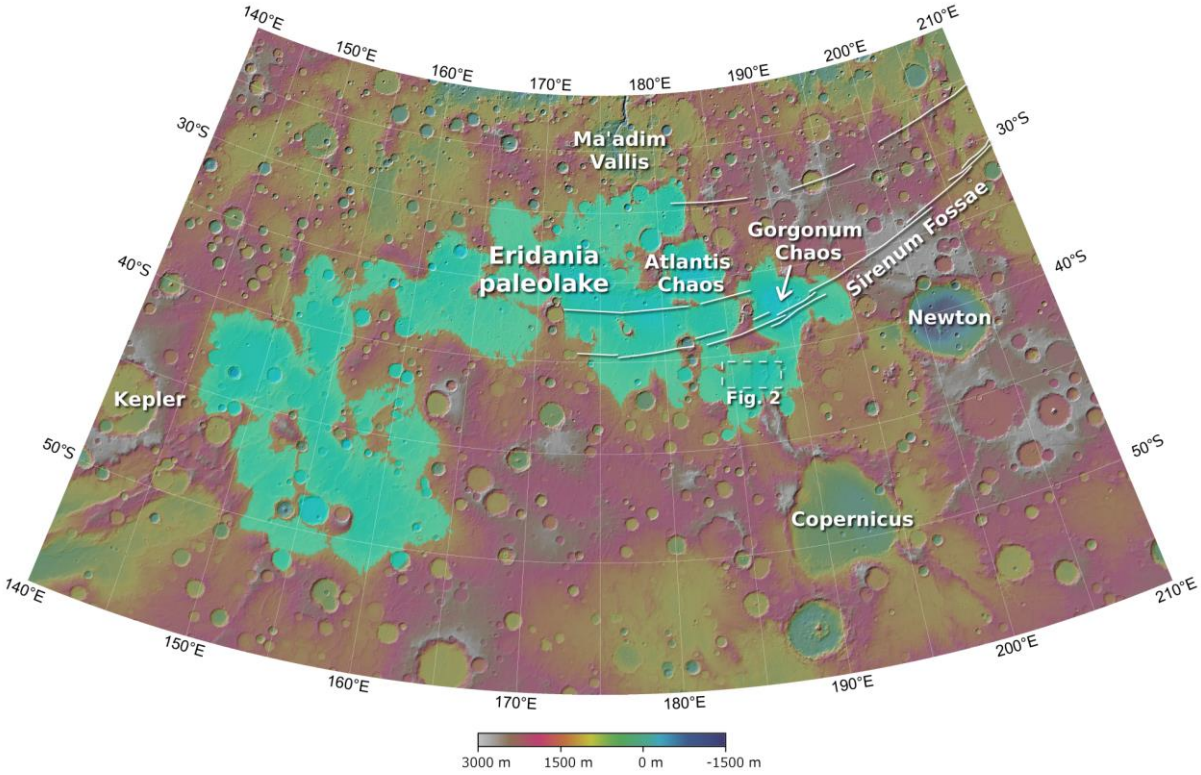

Figure 4.1: Regional map of part of the southern hemisphere on Mars. The cyan colour delineates the extent of the proposed Eridania Lake based on the 1100 m contour. Position of investigated area is marked by dashed box and clearly the area lies inside the proposed borders of the former lake. Base map is MOLA DEM.

Gwinner et al., 2010). For detailed topographical analyses, we also used single shot data from the MOLA PEDR (Precision Experimental Data Record) data which we superposed on CTX images using ESRI ArcGIS 10 software. This software was also used to merge all available datasets. The data were projected in a sinusoidal projection with the central meridian set at 187°E to minimize geometric distortion.

Absolute model ages were determined from crater size–frequency distributions, utilizing the software tool *CraterTools* (Kneissl et al., 2011), which ensures a distortion-free measurement of crater diameters independently from map projection, and the software *Craterstats* (Michael and Neukum, 2010) applying the production function of Ivanov (2001) and the impact-cratering chronology model of Hartmann and Neukum (2001). The mapped

crater population was tested for randomness to avoid the inclusion of secondary crater clusters (Michael et al., 2012). Craters were counted on CTX images.

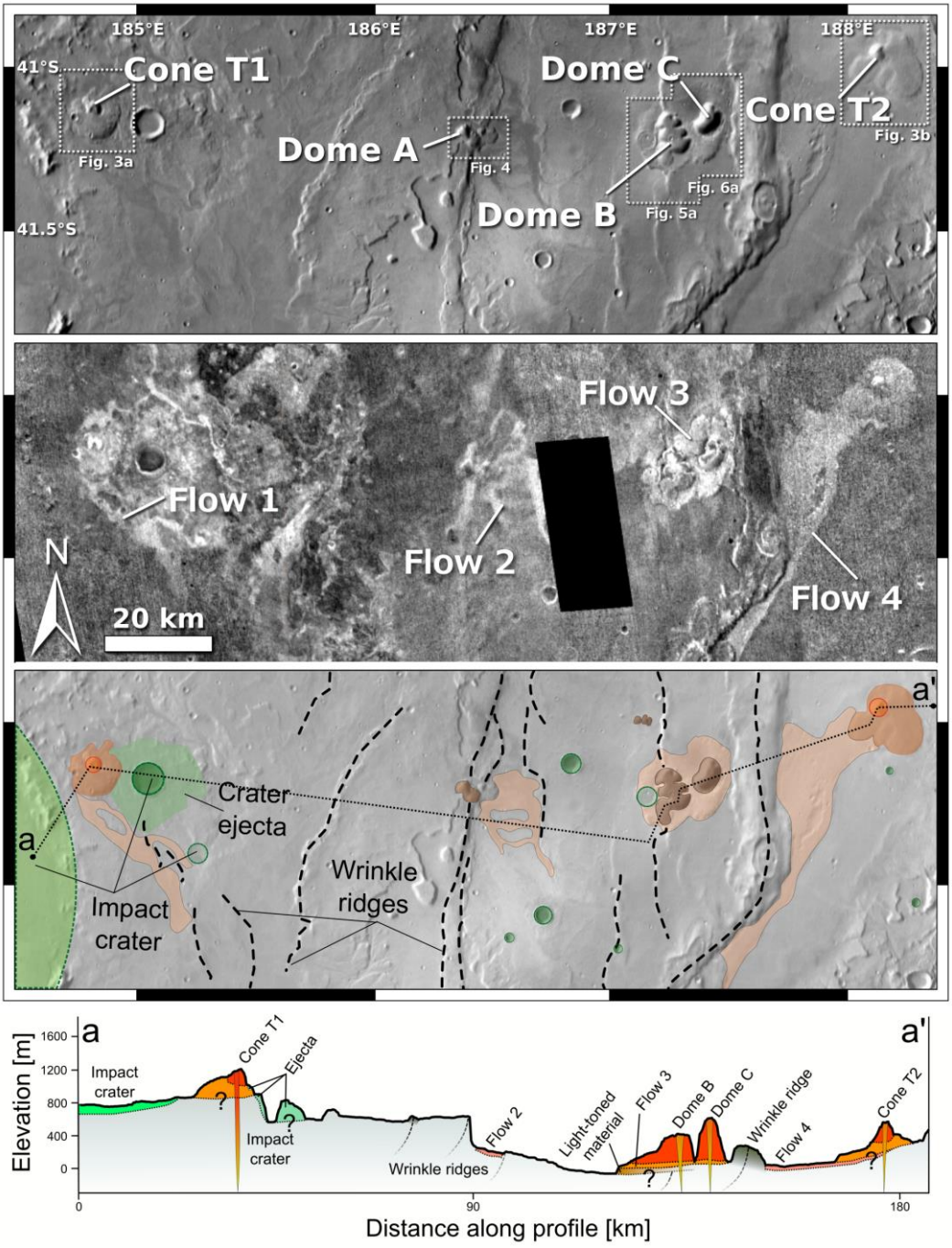

Figure 4.2: THEMIS-IR daytime (upper image), nighttime (middle) and interpretational map of the study area (bottom image). The thermal contrast between the two upper images suggests the presence of flow structures associated with cones and domes. Note the wrinkle ridges crossing the basin. The cross-section shows the stratigraphic relations of the investigated edifices with underlying units. Profile based on MOLA DEM and position marked by dotted line in bottom image.

Table 4.1: List of THEMIS images used in this study.

THEMIS image	Local Solar Time (Max)	Edifice(s)
I06941002	5.565556	Cone T1, Flow 1
I10885002	4.965	Dome A, Flow 2
I14554012	5.926667	Flow 2 and 3
I34557006	3.509167	Dome B, C, Flow 3
I06504011	5.643333	Dome B, C, Flow 3
I06142003	5.623055	Dome B, C, Flow 3
I22828008	5.975555	Flow 4
I06504011	5.643333	Flow 4
I34532006	3.536944	Cone T2

4.3. Regional setting

The study area is located in Terra Sirenum, a highland region which is crossed by approximately E-W-trending Tharsis-radial graben systems propagating from Arsia Mons over a distance of ~3,700 km. These grabens may represent the surface expression of volcanic dykes (Wilson and Head, 2002). Several wrinkle ridges, commonly interpreted as fault-propagation folds (e.g., Mercier et al., 1997; Schultz, 2000), indicate contractional deformation. The study area lies within the borders of the proposed former Eridania paleolake (Irwin et al., 2004; Fig. 4.1), a possible source for the formation of the Ma'adim Vallis outflow channel.

At local scale, the area is found within an unnamed depression (centred 41.40°S, 186.80°E) of unknown origin. Several conical and domical landforms (marked on Fig. 4.2a) are located within an area (~150 km × ~30 km) elongated in E-W direction. Except for one edifice (Cone T1), the remaining edifices are situated inside another, more localized unnamed depression. The margins of this depression are roughly 500 m in elevation above Mars' global datum (MGD). Based on HRSC (High Resolution Stereo Camera) Digital Elevation Models (DEMs), the lowest point (40 m below MGD) is situated close to the southwestern edge (41.35°S, 187.17°E) of Dome B, where a distinctive light-toned scarp is visible.

The depression is cut by several wrinkle ridges with a sinuous trace in plan-view. The wrinkle ridges stand several tens of meters above the surrounding plains, and Domes A and B appear to be superposed on two separate wrinkle ridges. Cone T1 is situated ~850 m above MGD near the edge of a highly eroded, ~110 km diameter impact crater infilled by younger deposits. The edifices are associated with flow landforms as visible in the HRSC and CTX images.

4.4. Results

4.4.1. Thermal properties

Several regions of enhanced relative thermal radiance are visible in the nighttime THEMIS (Thermal Emission Imaging System) infrared images (Fig. 4.2a, b; see Tab. 4.1 for THEMIS image details). The five brightest patches correspond to the locations of the studied small-scale edifices (marked as Cones T1 and T2 and Domes A, B, and C in Fig. 4.2a) and associated flow features (marked as 1, 2, 3, and 4 in Fig. 4.2b). The two conical (Cones T1 and T2), and three dome-shaped edifices (Domes A, B, and C), display steep, lobate margins visible in daytime THEMIS images. Except for Flow 3, the flows are elongated with partially anabranching channels visible in THEMIS day- and night-time images. Flow 3 is different in that it surrounds domes B and C to an approximately constant radius, rather than being elongated. In contrast, Flow 4 is clearly visible on THEMIS night-time images and can be traced for about 50 km in a southern direction. Flow 2 and 4 can be traced to point-like sources, Dome A and Cone T2 respectively, whereas Flow 3 cannot be directly related to either Dome B or Dome C. Flow 1 may also be linked to a point-like source area (Cone T1); but more flows are visible that originate around a ~6 km impact crater (centred at 41.17°S, 185.07°E). The floor of this 6-km diameter crater is characterized by low relative

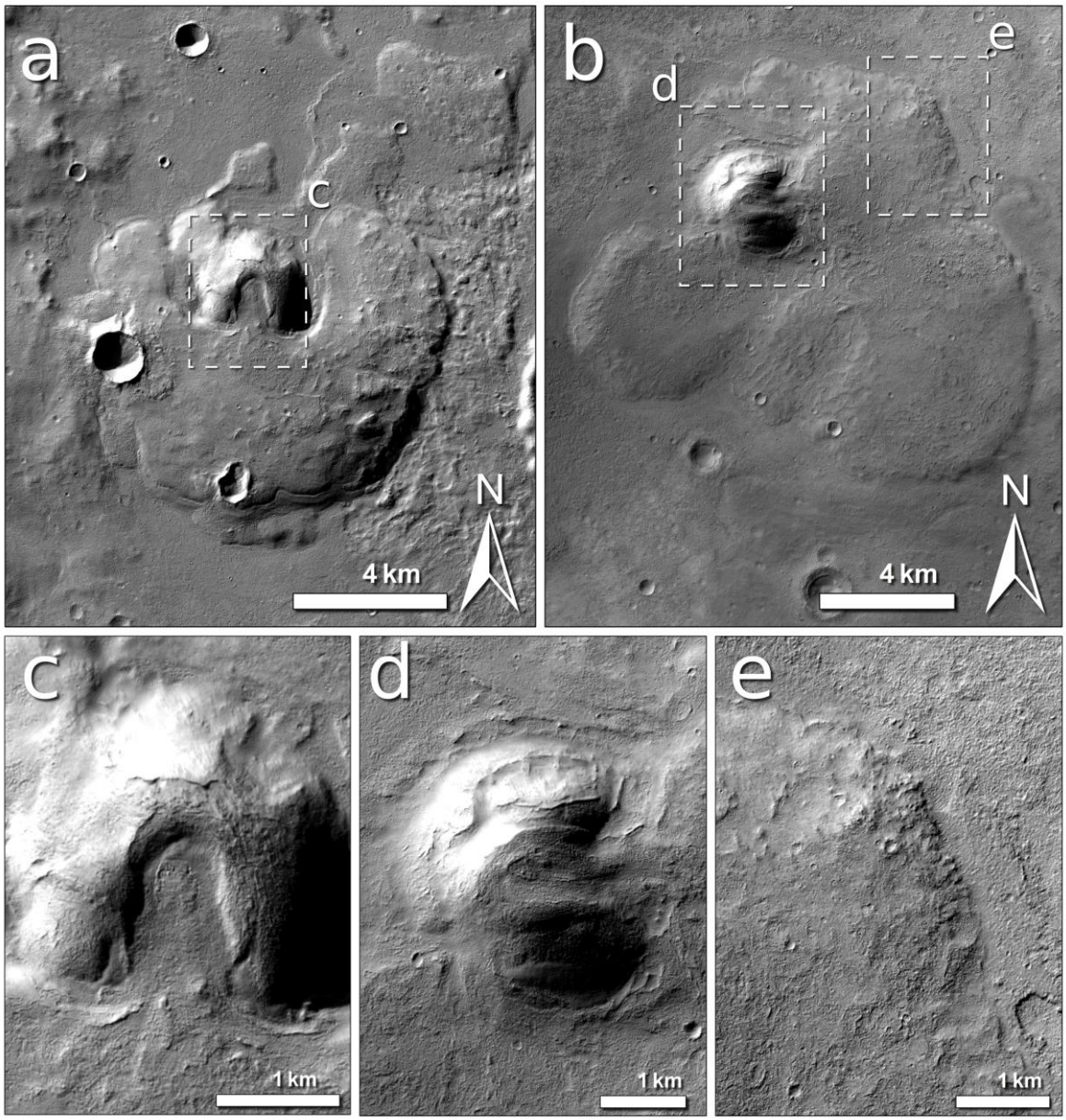

Figure 4.3: Two cones (a,b) with associated flow aprons; note details of cones (c,d) with central vent from flow aprons material erupted to the surface. (e) is showing edge of overlapping flow aprons. See also Fig. 4.2 for position within investigated area. CTX images B18_016835_1386 (a), and mosaic of CTX images B19_016914_1399 and P16_007117_1362 (b), centred 41.15°S, 184.84°E and 41.00°S, 188.15°E, respectively. Image credit NASA/JPL/MSSS.

thermal radiance, as are those of other large impact craters in the study area. The low thermal emission is also visible on the north-facing edge of this crater in contradiction to the domical and conical edifices, where north-facing slopes have higher thermal emission in THEMIS nighttime images.

4.4.2. Morphology

Cones T1 and T2 are shown in Figure 4.2. Both cones are breached to the south and east, respectively (Fig. 4.3a, b), and are associated with flow aprons that partly cover the lower flanks of the cones. The western cone T1 (Fig. 4.3a, 41.13°S, 184.85°E) measures about 3 km in diameter and 230 m in height, based on data acquired through the Mars Orbiter Laser Altimeter (MOLA). A central summit depression is breached towards the south and a small mound from where the flow apron originates is visible (Fig. 4.3c). The flow apron is ~8.5 km wide and spreads as a single, compact unit around the cone, except in the north. The southern edge of the flow apron is relatively steep, as demonstrated by cast shadows and younger talus aprons partly hiding the edge itself. Based on single MOLA shot data, the flow apron is between 100 and 130 m thick and the steepest slopes are ~10° to 11°; however, they can reach up to 20° after the talus is numerically removed by taking values of neighbouring MOLA shots not influenced by talus. The surface of the flow apron is superposed by two small impact craters (with diameters of ~1.3 km and ~0.8 km) without distinctive fluidized ejecta features. The eastern Cone T2 (Fig. 4.3b, 40.945°S, 188.11°E) is similar in size (~3 km in diameter and ~290 m high), but lacks a deep summit depression, although the cone itself is breached towards the east. Its flanks appear partly degraded, especially in the northern part of the cone. No vent sources can be distinguished on the cone flanks. The flow apron extending from the cone is ~12.5 km long in the north-south direction, forming four distinct lobes. Overlapping flow apron margins suggest multiple formation events (Fig. 4.3e). Compared to Cone T1, the flow aprons around Cone T2 do not have such steep margins (between 3° to 5°) and they are morphologically less distinct compared to their surroundings. These flow aprons cover the source of Flow 4 that propagates for ~50 km in a southwestern direction. Flow 4 is between ~1 km and ~8 km wide and between ~30 m and 50 m thick. The flow was impeded to the west by a wrinkle ridge causing flow deflection towards

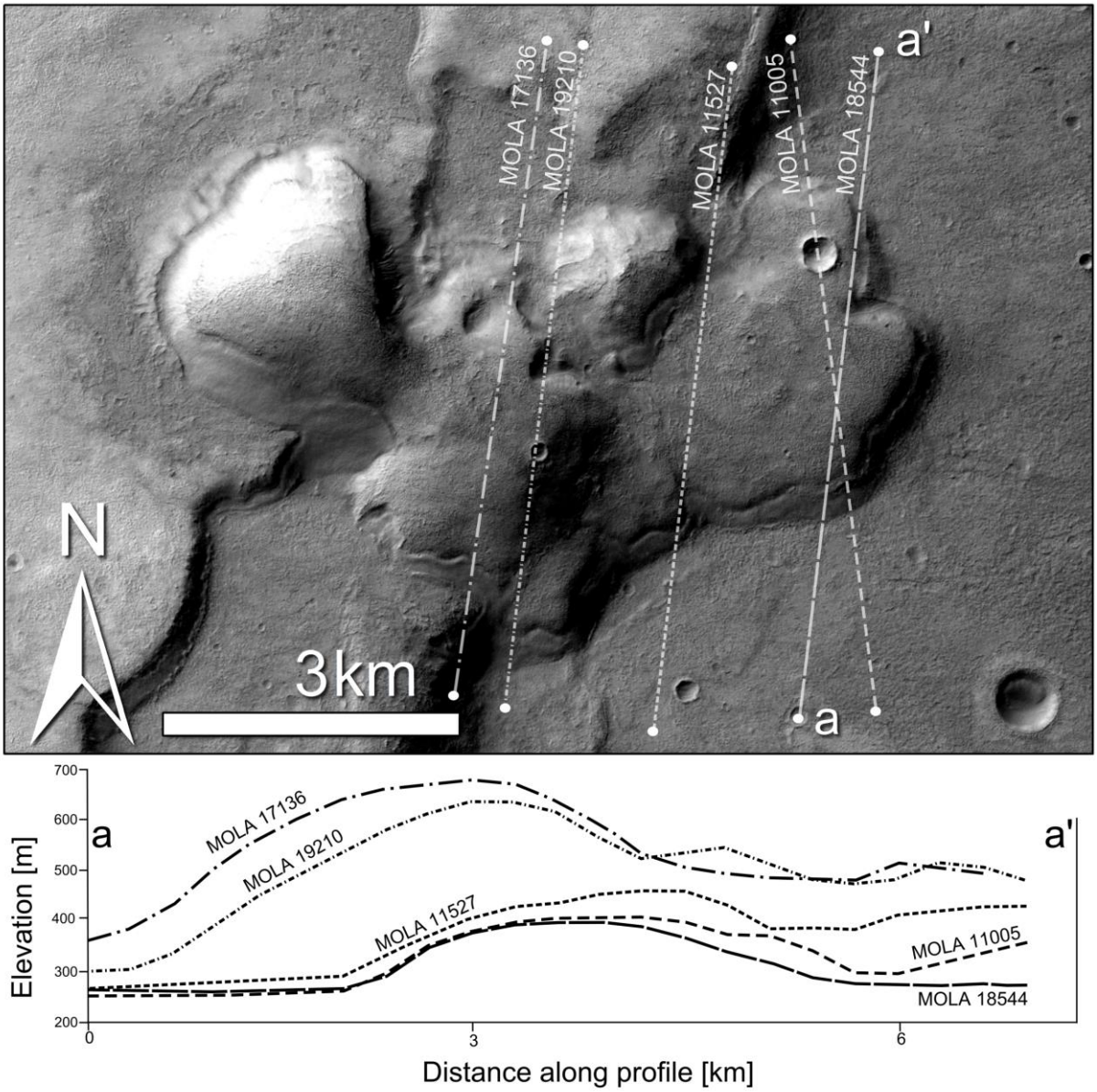

Figure 4.4. Image of Dome A with marked MOLA PEDRs and associated topographic profiles. Part of the Dome A seems to collapse and propagate in eastern direction. See Fig. 4.2 for position within investigated area. Based on CTX image D16_033331_1391, centred 41.21°S, 184.44°E.

the south. The flow margin is relatively rugged with many small-scale lobes and the surface exhibits rough texture partially softened by mantling deposits.

In the central part of the study area, three dome structures are associated with flows (Fig. 4.2a, b). Two of them are covered by CTX and HiRISE images (Domes B and C) whereas Dome A is covered by CTX only. Dome A (Fig. 4.4, 41.20°S, 186.40°E) is

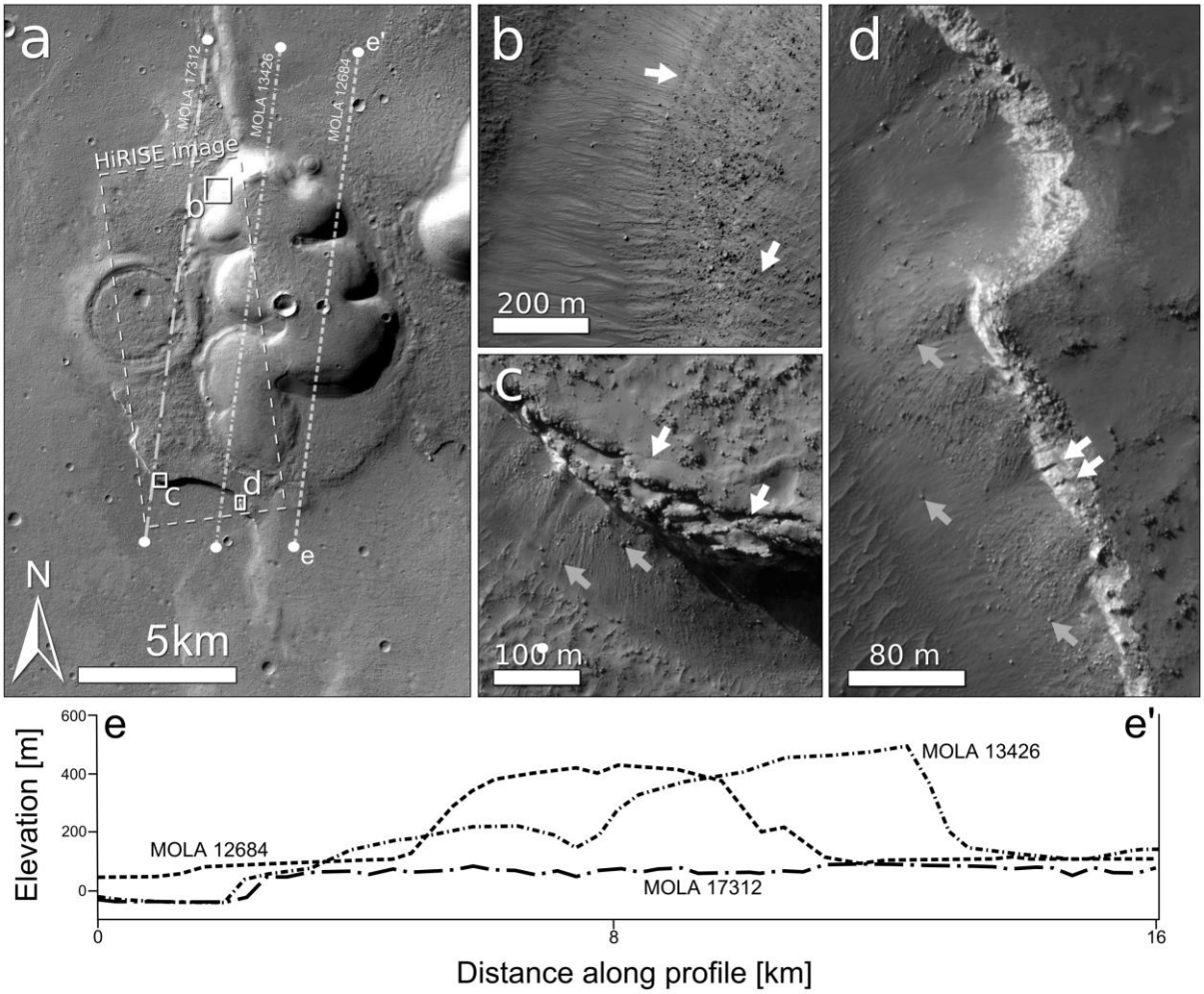

Figure 4.5: Image of Dome B with close up details. (a) Detail of Dome B and surrounding flow and marked position of HiRISE image ESP_033977_1385 with marked positions of MOLA PEDRs and associated topographic profiles. Based on CTX image G19_025696_1389, centred 41.22°S, 187.24°E. (b) Detail of HiRISE image showing the contact between the northwestern edge of the dome and the underlying unit. Large boulders forming dome itself and aeolian deposits at the top of the dome together with modification by gully activities are clearly visible. (c) Detail of the bedrock on which Dome B is superposed on as exposed by a ~80 m high scarp. Pristine fracture morphologies suggest ongoing scarp erosion. Note that the talus is mainly formed by fine-grained material and small amounts of boulders less than ~6 metres large (marked by gray arrows), larger blocks are missing. The tensile fractures parallel to the scarp in the capped unit (marked by white arrows) are similar to fractures associated with rotational block-fall landslides known from Earth. (d) Detail of HiRISE image showing another part of the scarp. Again, no large blocks of fallen rocks are visible and the talus is composed mainly of finer particles and smaller boulders (marked by gray arrows). Two white arrows indicate small grooves, which might have formed by ongoing aeolian erosion. These grooves show that the exposed material is susceptible to erosion. Image credit: NASA/JPL/UofA and NASA/JPL/MSSS.

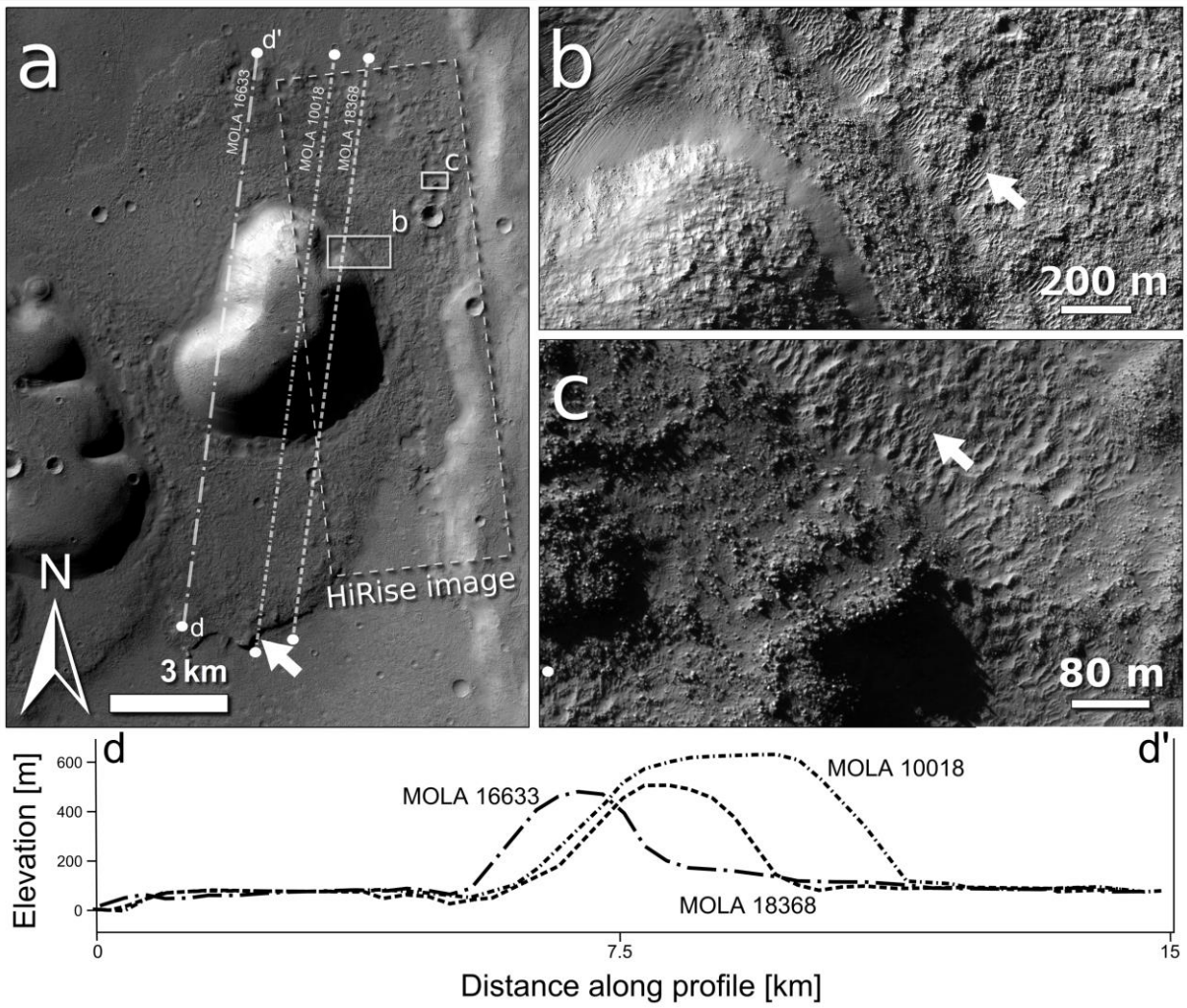

Figure 4.6: Image of Dome C and surrounding flow. (a) The dome edifice (Dome C, see Fig. 4.2 for position) is clearly surrounded by a flow structure that has steep edges, as demonstrated by the shadows on the southern margin. White arrow marks scarp on the edge of Flow 3. Position of MOLA PEDRs marked by lines and HiRISE image ESP_026474_1385 marked by dashed rectangle. Part of CTX image B18_016769_1369, centred 41.15°S, 187.4X°E. (b) Detail of HiRISE image covering part of dome flanks (left part of image b) and flow structure (right part). Note large boulders forming the dome itself and aeolian deposits forming Transverse Aeolian Ridges (marked by white arrow). (c) The edge of the flow structure on the border with surrounding older, flat layer. The margin of the internal flow is formed by large-scale boulders that are partly covered by aeolian material (marked by white arrow). The older unit contains small Transverse Aeolian Ridges (Balme et al., 2008). Image credit NASA/JPL/UofA and NASA/JPL/MSSS.

a ~2.5 km wide mound superposed on a wrinkle ridge. A ~5 km long and over ~300 m high flow apron propagating in the south-eastern direction and appears to be associated with Dome A. The flanks of the flow apron have slope angles between 7° and 11°. The other two domes,

marked as Dome B (Fig. 4.5a, 41.19°S, 187.26°E) and Dome C (Fig. 4.6a, 41.16°S, 187.41°E), are ~5 km × 7 km and ~3.5 km × 6 km in size and have maximum heights of 390 m and 530 m, respectively. Their flanks have slopes between 17° and 23°. Topographic data also reveal that the height of both structures decreases towards the south. For example, the highest part of Dome C is located close to its northern edge and is ~170 m higher than the southwestern part. Dome B is superposed on a wrinkle ridge, and the southwestern edge of the dome extends over a short distance to the south along the crest of the wrinkle ridge. The shape of Dome B is more irregular in plan-view compared to Dome C. Dome B exhibits four valleys dividing the dome into four differently-sized portions in plan view.

HiRISE images show that the cones, domes, and associated flow features have bouldery surfaces that are partly covered by younger, fine-grained deposits which infill/occupy the spaces between the exposed boulders. These deposits are less frequent at the steeper edges, where more exposed boulders are seen. The flanks seem to be irregularly layered (Fig. 4.5b, marked by arrows) and contain widely spread shallow gullies in the middle to lower flanks (Fig. 4.5b), which predominantly occur on the western edges. The northern and northeastern part of Dome C are not covered by younger draping material, enabling observations of the contact between flanks and surrounding flow units. The dome seems to be superposed on these units (Fig. 4.6b). Both Domes B and C are surrounded by flow features composed of one or more individual flow units. These flows are superposed on the underlying surrounding unit, which is heavily covered by impact craters in different stages of degradation and covered by a single layer, as demonstrated by the topographic relationship and abrupt transition between the units (e.g., Fig. 4.6c). Also, small ridges and wrinkles forming flow textural patterns are partly visible on the top of both domes (Fig. 4.5a, 4.6a), with inferred flow directions following the local topographic gradient.

The western margin of the flow unit around Dome B is disrupted by a ~3 km impact crater that is almost completely infilled by boulder-rich material. The south-western and southern margins are characterized by light-toned scarps with significant vertical offset (around 80 m at the southern margin of Dome B, based on single MOLA shots). A similar scarp, but with lower vertical offset, is also seen at the southern edge of Dome C (marked by a white arrow on Fig. 4.6a). The scarps show signs of ongoing erosion, as evidenced by talus, falling rocks with boulder trails in the talus, linear to arcuate fractures parallel to the scarp edge (marked by white arrows on Fig. 4.5c), and small grooves (marked by white arrows on Fig. 4.5d). The grain size of talus material at the base of these scarps is too small to be resolved in HiRISE imagery (25cm/pixel), although a small portion of larger boulders is visible (marked by gray arrows on Figs. 4.5c,d). HiRISE images reveal that the surface and margins of the domes and their surrounding flows are composed of boulders up to several meters across (Figs 4.5b and 4.6b,c), and are partly covered by aeolian deposits forming Transverse Aeolian Ridges (e.g., Balme et al., 2008; marked by white arrows on Fig. 4.6b,c). The boulder distribution is spatially random. Several impact craters with diameters of tens to a few hundred meters are superposed on the flow units. The interior floors of the craters also contain boulders of different sizes.

We note that, within the study area, a double-rimmed depression is observed on the top of a wrinkle ridge centred at 41.41°S, 187.64°E. The depression is elongated in a north-south direction and is 7.5 km × 4.5 km in size and contains a 3 km-diameter inner rim. The inner structure is circular in plan-view and exhibits a small central mound. The outer flanks of the depression do not show any evidence of impact ejecta deposits.

Several larger impact craters in the study area have floors filled by re-deposited material. This material originates on the crater flanks and the surface is characterized by flow-like pattern with elongated subparallel grooves and series of small depressions forming

knobby terrains in shape corresponding to ‘lineated valley fills’ and/or ‘concentric crater fills’ (Colaprete and Jakosky, 1998).

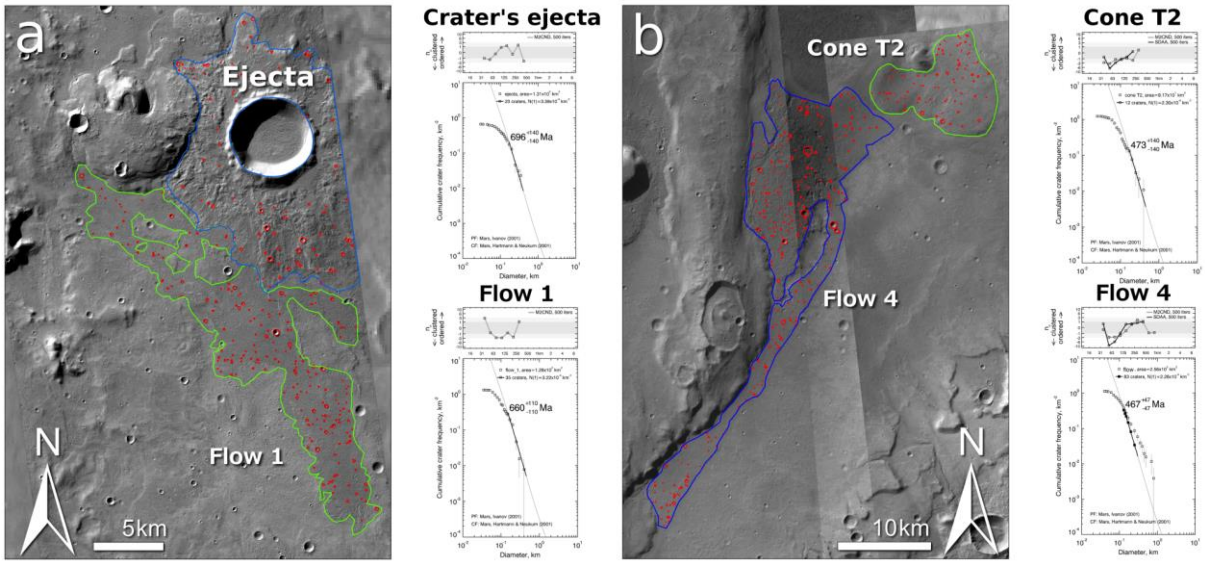

Figure 4.7: Absolute model ages of (a) the crater’s ejecta and Flow 1, and (b) Cone T2, and Flow 4. (a) The cumulative crater size-frequency curves indicate an absolute model age 660±100 Ma for Flow 1 and 700±100 Ma for the crater’s ejecta. (b) The cumulative crater size-frequency curves indicate an absolute model age of 470±100 Ma for Cone T2 and 470±50 Ma for Flow 4. Note the panels above the cumulative crater size-frequency plots represent the randomness analyses (cf. Michael et al., 2012). Background images are CTX images B18_016835_1386 and mosaic of P16_007117_1362, G18_025274_1388 and B18_016769_1369. Image credit NASA/JPL/MSSS.

4.4.3. Ages

The domes and cones do not represent suitable areas for the determination of crater size-frequency distributions (CSFDs) because they are too small in areal extent. Instead, we determined the CSFDs of four units (marked on Fig. 4.7) with known relative stratigraphic relationships (see cross-section in Fig. 4.2). The ejecta blanket from a ~6 km impact crater is partly superposed on the flow apron associated with Cone T1, hence, representing a younger surface than the cone itself and the associated flow apron. From the ejecta material we determined an absolute model age of 700±100Ma. The source of Flow 1 is not exposed but may be covered by the ~1.3 km diameter impact crater on the western margin of the flow

apron associated with Cone T1. The formation age of Flow 1 is determined to be 660±100 Ma. The flow apron associated with Cone T2 appears to have formed at 470±100 Ma. Stratigraphically, Flow 4 is older than the apron thereby bracketing the age of volcanic activity. Based on the measured CSFD, Flow 4 formed at about 470±50 Ma.

4.5. Discussion

4.5.1. Infrared images

The investigated edifices and associated flows are brighter in infrared nighttime images relative to the background plains materials. By contrast, the floors of larger craters are darker (Fig. 4.2) than their surroundings. Areas covered with dust, unconsolidated or high-porosity materials cool down quickly after dusk, and hence, appear darker in infrared nighttime images (low thermal inertia), whereas exposed bedrock or boulder surfaces store the heat longer and appear brighter (high thermal inertia; Fergason et al., 2006). HiRISE images of the high relative thermal radiance areas show coarse material including meter-sized boulders (Figs. 4.5, 4.6). Dark areas with low relative thermal radiance in nighttime images are characterized by pitted and irregular terrain with/without a thick dust cover. However, it is noted that significant changes in local slopes can contribute to thermal signature variations (Fergason et al., 2006) due to differential insolation. Therefore, during the day, sunlit slopes accumulate more heat than shady slopes, which might be visible as brighter spots on nighttime THEMIS images as more heat is released. For this reason, the brighter areas on cones and domes may be related to steep flanks, rather than a higher thermal capacity. If the associated flow aprons and flows are taken into account, however, this explanation cannot account for all observed variations in nighttime thermal infrared image brightness, because the flow aprons and flows are brighter than their surroundings despite having similar slopes as the surrounding units. Hence, THEMIS nighttime infrared images suggest

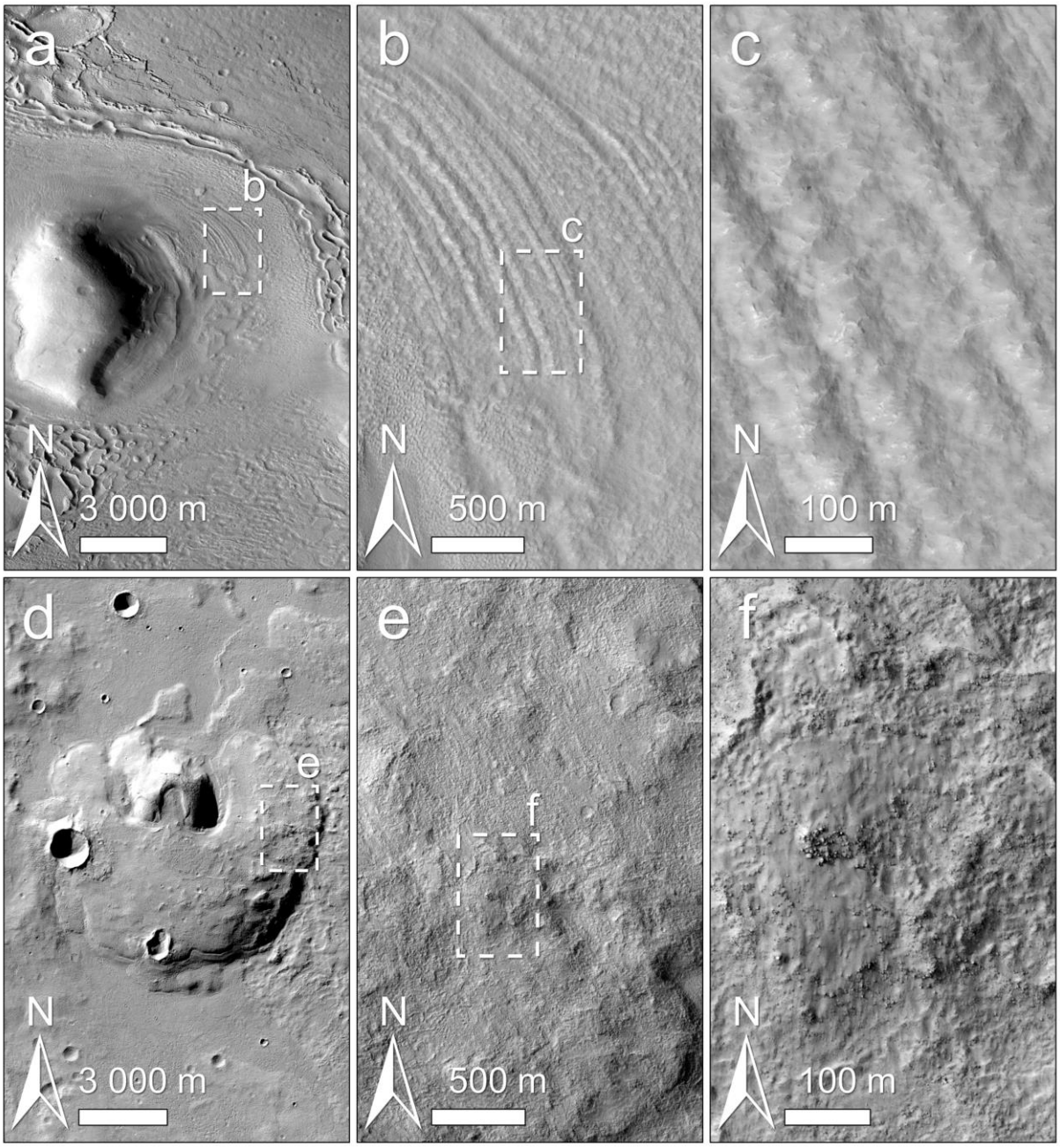

Figure 4.8: Examples of textures of lobate debris aprons at northern latitudes (a-c) and investigated flow aprons associated with Cone T1 (d-f) in various scales. Lobate debris aprons mainly miss significant amount of large boulders (c) which are clearly visible on investigated flow aprons (f) Lobate debris aprons associated with massif in Deuteronilus Mensae (a - part of CTX image D04_028840_2240_XN_44N334W , centred 44.067°N, 25.643°E, b-c based on HiRISE image ESP_037556_2245). (d) The flow apron associated with Cone T1 (d - part of CTX image B18_016835_1386_XI_41S175W, centred 41.13°S, 184.85°E, e-f based on HiRISE image ESP_037511_1385).

that the investigated features are indeed composed of consolidated materials or represent unconsolidated units with high proportions of dense (high thermal inertia) clasts.

4.5.2. Morphology

The domes stand several hundred meters above the surroundings plains and are partially superposed on wrinkle ridges. They exhibit well-preserved shapes and neither the cones nor the domes show much evidence for significant erosion (except a few small gullies), yet the morphological interpretation is not straightforward and depends upon the regional context. The study area is located in the southern mid-latitudes (around 40°S), where glacial and/or periglacial activity has produced a range of ice-related landforms (e.g., Squyres and Carr, 1986; Souness and Hubbard, 2012). For example, Squyres and Carr (1986) suggest that the martian regolith is deformed by quasi-viscous flow due to creep deformation of ice, a process known as 'terrain softening' (Jankowski and Squyres, 1992). A characteristic class of landforms related to this process are lobate debris aprons (Squyres, 1978), which in some ways have similar morphologies to the flow aprons around cones T1 and T2. However, several aspects make it unlikely that cones T1 and T2 are surrounded by lobate debris aprons.

Lobate debris aprons (LDA) are thought to be debris-covered glaciers, consisting of relatively pure ice (Hauber et al., 2008; Holt et al., 2008; Plaut et al., 2009) under a protective cover (Head et al., 2010). They commonly display distinct surface textures (Figs. 4.8a,b,c) that are indicative of subsurface ice and/or degradational processes such as sublimation. Key geomorphic features typically observed on the surfaces of LDA include the initiation of flow lineations in protected alcoves, the coalescence of flow lineations and convex-up topographic profiles (see Levy et al., 2014 and references therein). Possible sublimation-related landforms on lobate debris aprons include fractures and a characteristic pattern of pits and buttes that are interpreted to result from the progressive removal

of subsurface ice by sublimation (Mangold, 2003). Chuang and Crown (2005) describe typical morphologies of LDA surfaces, and place them into a degradation sequence progressing from 'smooth' to 'pitted' to ridge and valley or 'knobby'. Other surface textures indicative of ice-rich viscous material are the so-called 'brain terrain' (Levy et al., 2010) and ring-mold craters, defined as concentric crater forms shaped like a truncated torus and thought to be the result of impacts into relatively pure ice protected by a thin regolith (Kress and Head, 2008).

Neither flow lineations nor ring-mold craters nor possible sublimation landforms can be observed on the surfaces of the lobe-like features around the investigated edifices (Figs. 4.8d, e, f). The progressive degradation morphologies identified by Chuang and Crown (2005) are also not seen. The only property that is consistent with an origin by the viscous flow of ice-rich material is the convex-up cross-sectional shape. Such shape, however, is far from being diagnostic for ice-rich substrate, as it is typical for any plastic deformation. The surface ages of the investigated lobes are inconsistent with an origin as lobate debris aprons: whereas lobate debris aprons are geologically recent landforms and have absolute model ages of typically less than ~500 Ma (e.g., Morgan et al., 2009; Baker et al., 2010; Hartmann and Werner, 2010; Parsons and Holt, 2014; Fassett et al., 2014), the surfaces of the lobes around the edifices in the study area display model ages at the end of this limit or >500 Ma. In addition, impact crater formation on an ice-rich target material would have formed single or multi-layered, lobate rampart ejecta. This is not observed (cf. western crater ejecta on Cone T1 flow apron; Fig. 4.3a). Cones T1 and T2 are breached and flow aprons seem to originate from the centres of craters on the top of the cones. This suggests that material likely extruded from the subsurface through the craters to the surface, rather than originated at alcoves on the flanks of the cones, as it is typical for flowing ice-rich material (Head et al., 2010). A simple comparison between observations and expected characteristics

of lobate debris aprons illustrates that an origin of the aprons by the flow of ice-rich material is highly unlikely. Therefore, we exclude in the following the possibility that the lobes consist of an ice-rich substrate covered by a thin layer of regolith.

The inspection of HiRISE images reveals that Cone T2, Domes B and C, and Flows 2 and 3 contain apparently randomly distributed, meter-sized boulders (Fig. 4.5, 4.6). There is no obvious sorting of large boulders, suggesting that the flows are able to carry (and/or form) boulders over their entire length. This homogeneous distribution of boulders is inconsistent with glacial or periglacial processes, where boulders are often aligned or concentrated by flow or into moraines (Boulton, 1978; Arfstrom and Hartmann, 2005) and organized into patterned ground (Washburn, 1956). It is also inconsistent with the formation of gravity-driven rock avalanche deposits where variations in block sizes occur downslope in flow direction (Bulmer et al., 2005; Platz et al., 2012). In contrast, the apparent random distribution of boulders at the surface is consistent with some terrestrial lava flows (Bulmer et al., 2005), whose blocky nature is typically attributed to higher viscosities of the erupted magma.

The southwestern margin of Flow 3 is marked by a ~80 m-high scarp which exposes what appears to be bedrock. The exposed bedrock is relatively light-toned in the stratigraphically lower parts and is capped by a dark layer of massive material topped by boulders (see topographic profile in Fig. 4.2), which we interpret to be a resistant lava carapace. The scarp appears to be undergoing active erosion, as inferred from talus accumulation, rock fall (Fig. 4.5c, d), and occasional sharply-expressed fractures or clefts in the scarp (marked by white arrows on Fig. 4.5d). In addition, well-visible tension fractures with an orientation parallel to the scarp are visible in the cap unit (marked by white arrows on Fig. 4.5c), and are similar to fractures associated with rotational block-fall landslides on Earth. Interestingly, the amount of large boulders released from the scarp by rock fall appears to be limited, as only a few can be observed as part of the talus (marked by gray

arrows on Fig. 4.5c, d). This suggests that the exposed light-toned material is less competent and presumably fine-grained, so that the boulders are quickly (in geological terms) broken into smaller pieces or break up upon impact.

Due to a lack of spectroscopic observations with appropriate spatial resolution, we can only speculate about the composition, and hence, the origin of the cliff-forming material and scarp. Two scenarios seem to be plausible: (i) the bedrock might be composed of sedimentary rocks deposited in a lacustrine environment and/or formed by aeolian processes, or (ii), by weakly consolidated tephra (e.g., tuff, scoria, ash) or welded pyroclastic-flow deposits (i.e., ignimbrites) formed by explosive eruptions. Explosive magmatic fragmentation occurs when the pressure in the interconnected bubble-melt network exceeds the load of overlying rocks or through the interaction of ascending magma with surface/subsurface water and/or water ice (cf. phreatomagmatic fragmentation). Both fragmentation processes would cause dispersion and subsequent accumulation and deposition of fragmented material in the close vicinity of the vent. Once the source of fragmentation is depleted, volcanic activity would change in style from explosive into effusive, perhaps causing the formation of a resistant lava unit partly overlying the weaker sedimentary bedrock. However, based on current data, we cannot rule out the possibility that the dark resistant lava unit propagated over sediments of non-volcanic origin. In both scenarios, though, the more resistant dark lava unit protects the easily erodible bright bedrock. The scarp itself might be the result of magma intrusion into shallow sub-crustal levels causing doming of the overlying rocks. Another mechanism might be aeolian erosion removing bright material from the edges of a sedimentary unit partially capped by dark lavas in those areas where the sediments were not protected by the resistant lava unit. Ongoing erosion would then lead to undermining of the more resistant capping unit and scarp formation. Finally, the scarp might have formed as a result of both mutually active processes.

The entire area is covered by thin layer(s) of very fine-grained deposits draping the original surface textures. Such deposits are common on Mars at latitudes between 30° to 60°, where they form 1-10 m thick, ice-rich layers (Mustard et al., 2001). Layers of these very fine-grained deposits are partly missing at the steep edges of the investigated edifices where boulder-rich surfaces are present, again indicating active erosion.

4.5.3. Ages

Our crater counts suggest post-Noachian, probably Middle Amazonian, ages for the formation of the studied landforms; between 0.5 Ga to 0.7 Ga (Fig. 4.7). However, we are aware that smaller surface areas can bias the estimates towards younger ages (Michael and Neukum, 2010) which could introduce inaccuracies into the results. Therefore, we take established ages only in association with relative stratigraphy. Irwin et al. (2004) suggested that the Eridania paleolake was spread over this area during the Late Noachian/Early Hesperian. This conclusion is supported by Tanaka et al. (2014) who dated the unit on which the investigated cones and domes stand as Late Noachian in age. Another hint is recorded by the wrinkle ridges on which Domes A and B are superposed. The ridged plains were dated by Scott and Tanaka (1986) as Hesperian to Amazonian in age and by Greeley and Guest (1987) as Hesperian in age. Wendt et al. (2013) state that the ridged plains cannot have formed earlier than the fields of light-toned knobs filling most of the ancient basins in Terra Cimmeria/Terra Sirenum. These stratigraphic observations suggest that the cones, domes, and flows have to postdate the Early Hesperian Epoch, and are consistent with the notion based on crater statistics that the investigated landforms are mid-Amazonian in age.

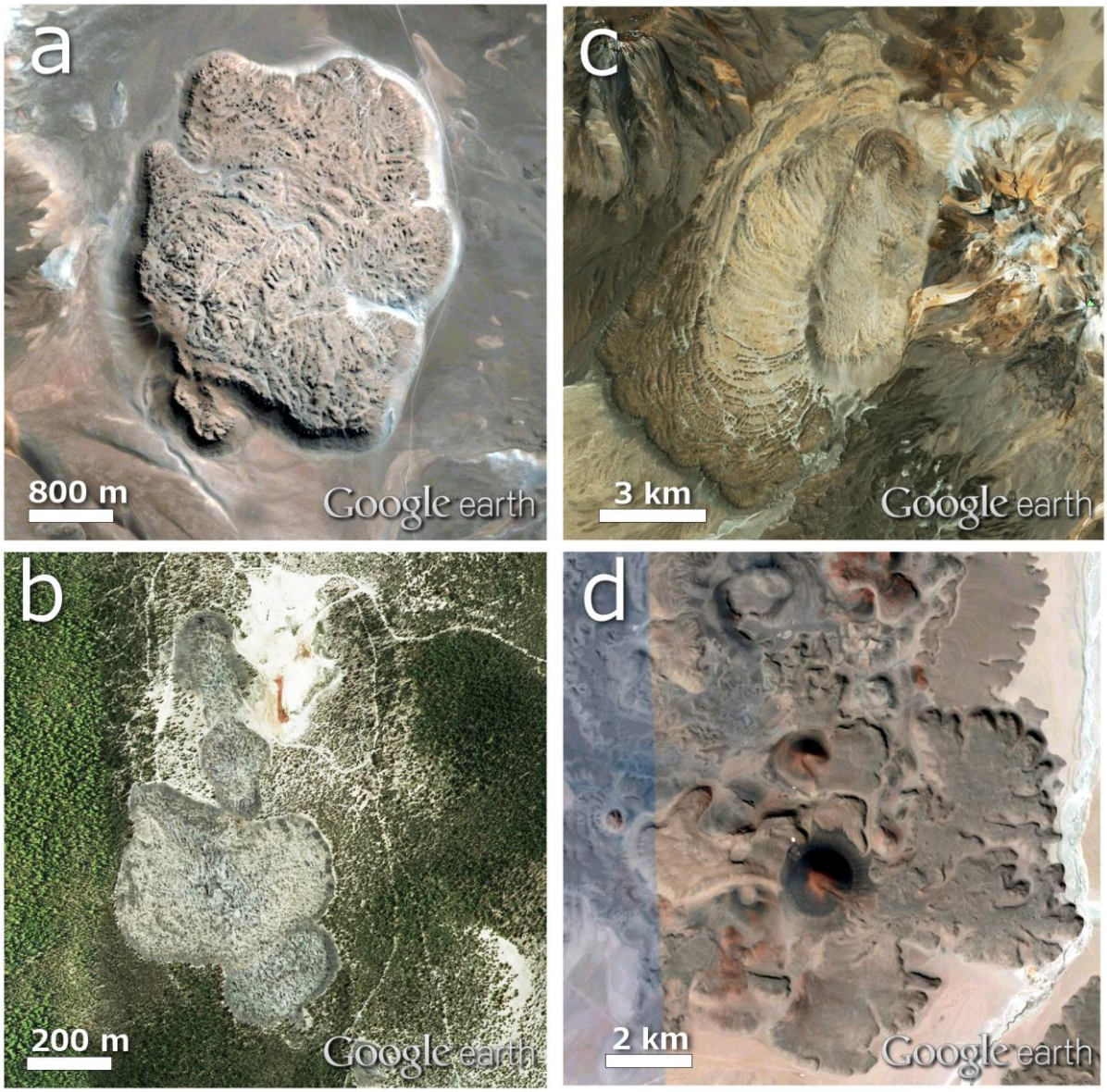

Figure 4.9: Examples of terrestrial lava domes/coulées (a,b,c) and a volcanic cone with associated lava flows (d), which might represent suitable analogues to investigated martian edifices. (a) Chillahuita, large dacitic lava dome in the Chilean Andes (22°8.356'S, 68°1.766'W; image credit: DigitalGlobe 2014) (b) Small lava dome (41°37.2'N, 121°31.5'W) to the North of the rhyolite and dacite obsidian flow known as Glass Mountain, part of Medicine Lake Volcano in California, USA. (c) Chao (22º07'S, 68º09'W, image credit: CNES/Spot Image), 14.5 km long dacitic coulée in Chile. (d) Small basaltic-andesite volcanic cone with outgoing flows situated north of the small village Antofagasta de la Sierra in Argentina (25º53'S, 67º24'W, image credit: Inav/Geosistemas SRL, CNES/Astrium). All images obtained via GoogleEarth™.

4.5.4. Interpretation and implications

Based on the combined morphological and infrared observations, we therefore conclude that volcanism seems to be the most probable explanation for the formation of the edifices and their associated flows. This conclusion is supported by the inspection of OMEGA based (Visible and Infrared Mineralogical Mapping Spectrometer) global maps (Ody et al., 2012), which suggest that exposed boulders atop Domes B and C and Flow 3 have low abundances of olivine and moderate amounts of pyroxene, favoring an origin related to volcanism rather than to water and/or water ice. The morphological similarities to terrestrial lava domes, coulées and obsidian flows (Fig. 4.9) raise the possibility that the studied features represent a suite of volcanic landforms associated with evolved magmas. The cones and associated lava flow aprons are morphologically different to previously observed small volcanic edifices on Mars such as scoria cones (Meresse et al., 2008; Brož and Hauber, 2012) and tuff rings/cones (Brož and Hauber, 2013). Instead, they may represent volcanic cones or collapsed steep-sided domes with associated viscous lava flow aprons which partly embay the cones themselves, a situation that is known from terrestrial coulées such as the 'Chao dacite' (Fig. 4.9c) in the Andes (de Silva et al., 1994). The flow aprons associated with the cones have steep margins (up to 20°), which is in stark contrast to less viscous basaltic flows in Tharsis or Elysium that are typically characterized by low relief and very gentle flank slopes (Hauber et al., 2009). The differences in flow apron thickness compared to flow thickness suggest changes in flow rheology during cone formation and associated flow emplacement, and may be directly linked to differing rates of degassing and/or magma cooling histories. The absence of volcanic craters in association with the investigated edifices also suggests that the dominant style of volcanism was effusive rather than explosive.

The implications of young volcanism in the martian highlands is in agreement with new petrological modeling results. Baratoux et al. (2013) showed that a transition occurred from the Noachian to the Hesperian and Amazonian where in the former primarily low-Ca pyroxene assemblages formed, whereas the latter (i.e., Hesperian and Amazonian periods) are dominated by high-Ca pyroxene occurrences, in accordance with orbital spectroscopic observations. Extrusion of low-volume volcanic materials, which formed the studied edifices, suggests storage of evolved magmas at shallow sub-crustal level(s). Such small magmatic bodies are unlikely to ascend from greater depth or from the crust-mantle boundary. Magmatic differentiation towards more evolved compositions is more likely to occur through multiple stalling and ascending phases, at least as known from terrestrial settings (e.g., Platz et al., 2012). New density constraints of the martian crust (Baratoux et al., 2014), based on martian meteorites, in situ analyses of igneous rocks, and surface element abundances from orbital Gamma-ray spectrometers, reveal higher densities (>3100 $kg.m^3$) than the conservative values used for crustal thickness modeling (2700 – 3100 $kg.m^3$). This finding also supports our interpretation that the studied landforms represent volcanic constructs. Higher crustal densities favour the buoyant ascent of even small magmatic bodies and their eruption onto the surface.

4.6. Conclusions

We have identified small-scale volcanic edifices in the southern highlands of Mars that have a relatively young Amazonian age. The steep-sided morphology suggests that highly viscous lava formed them, magma intruding into the crust causing doming and extruding onto the surface or vice versa. If so, volcanic edifices composed of evolved magmas may not only be present in the northern lowlands in Arcadia Planitia (Rampey et al., 2007), but also in the southern highlands, far from any known major volcanic centres. The proposed

explanation for cryptodomes in Arcadia Planitia (Farrand et al., 2011), in which magma viscosity increased due to magma degassing and/or a high degree of crystallization, may be also be valid here. Although decompression-induced degassing and/or crystallization changes the magma's composition, it remains open as to how differentiated the magma is that formed these volcanic domes and cones. The extrusion of small-volume differentiated lava onto the surface implies multiple storage levels during magma ascent through a thick, southern highland crust. Our observations and conclusions expand our knowledge about evolved magmas on Mars, which seem to be more widespread than previously thought (Wray et al., 2013; Meslin et al., 2013; Carter and Poulet, 2013; Sautter et al., 2014). Further investigations are required to elucidate the origin of these edifices; they clearly represent ideal candidates for detail spectroscopic observations.

Acknowledgements

We appreciate the efforts of the instrument teams (MOLA, THEMIS, HRSC, CTX, HiRISE) who acquired and archived the data used in our investigation. Especially, we would like to thank W. Brent Garry for his constructive comments on a previous version of this manuscript, and the HiRISE team which provided new interesting observations on our requests. These data greatly improved our study. We would like to also thank to David A. Williams and an anonymous reviewer for their suggestions how to improve our study and to Christophe Sotin for handling the manuscript throughout the editorial process. Petr Brož was a visiting research student at the Open University, UK, when this research was undertaken. This study was supported by the Grant No. 580313 from the Grant Agency of Charles University in Prague (GAUK) and by the Helmholtz Association through the research alliance 'Planetary Evolution and Life'.

References

Arfstrom, J. and Hartmann, W.K., 2005. Martian flow features, moraine-like ridges, and gullies: Terrestrial analogs and interrelationships. Icarus 174, pp. 321–335, doi: 10.1016/j.icarus.2005.05.011.

Baker, D.M., Head, J.W., Marchant, D. R., 2010. Flow patterns of lobate debris aprons and lineated valley fill north of Ismeniae Fossae, Mars: Evidence for extensive mid-latitude glaciation in the Late Amazonian, Icarus 207, 186-209, doi: 10.1016/j.icarus.2009.11.017.

Balme, M., Berman, D., Bourke, M. Zimbelman, J., 2008. Transverse Aeolian Ridges (TARs) on Mars. Geomorphology Journal, 101(4) pp. 703–720, doi: 10.1016/j.geomorph.2008.03.011.

Bandfield, J. L., Hamilton, V. E., Christensen, P. R., McSween, H. Y. Jr., 2004. Identification of quartzofeldspathic materials on Mars, J. Geophys. Res., 109, E10009, doi: 10.1029/2004JE002290.

Baratoux, D., Toplis, M. J., Monnereau, M., Sautter, V., 2013. The petrological expression of early Mars volcanism, J. Geophys. Res. Planets, 118, 59–64, doi:10.1029/2012JE004234.

Baratoux, D., Samuel, H., Michaut, C., Toplis, M. J., Monnereau, M., Wieczorek, M., Garcia, R. , Kurita, K., 2014. Petrological constraints on the density of the Martian crust, J. Geophys. Res. Planets, 119, 1707-1727, doi:10.1002/2014JE004642.

Bulmer, M.H., Glaze, L.S., Anderson, S., Shocky, K.M., 2005. Distinguishing between primary and secondary emplacement events of blocky volcanic deposits using rock size

distributions. Journal of Geophysical. Research. 110, B01201, doi:10.1029/2003JB002841.

Boulton, G.S., 1978. Boulder shapes and grain size distributions of debris as indicators of transport paths through a glacier and till genesis. Sedimentology 25, 773–799.

Brož, P., and Hauber, E., 2012. An unique volcanic field in Tharsis, Mars: Pyroclastic cones as evidence for explosive eruptions, Icarus, 218, 1, 88–99, doi:10.1016/j.icarus.2011.11.030.

Brož, P., and Hauber, E., 2013. Hydrovolcanic tuff rings and cones as indicators for phreatomagmatic explosive eruptions on Mars, JGR-Planets, Volume 118, 8, 1656–1675, doi: 10.1002/jgre.20120.

Carter, J., and Poulet, F., 2013. Ancient plutonic processes on Mars inferred from the detection of possible anorthositic terrains, Nature Geoscience 6, 1008–1012, doi:10.1038/ngeo1995.

Christensen, P.R. et al., 2004. The Thermal Emission Imaging System (THEMIS) for the Mars 2001 Odyssey Mission. Space Sci. Rev. 110, 85–130, doi: 10.1023/B:SPAC.0000021008.16305.94.

Christensen, P. R., et al., 2005. Evidence for magmatic evolution and diversity on Mars from infrared observations, Nature, 436, 504– 509, doi: 10.1038/nature03639.

Chuang, F. C, and Crown, D.A., 2005. Surface characteristics and degradational history of debris aprons in the Tempe Terra/Mareotis fossae region of Mars. Icarus, 179(1), 24-42, doi:10.1016/j.icarus.2005.05.014.

Colaprete, A., and Jakosky, B.M., 1998. Ice flow and rock glaciers on Mars. J. Geophys. Res. 103, 5897–5909, doi: 10.1029/97JE03371.

de Silva, S., Self, P., Francis, P.W., Drake, R.E., Ramirez, R.C., 1994. Effusive silicic volcanism in the Central Andes: the Chao dacite and other young lavas of the Altiplano-Puna Volcanic Complex. Journal of Geophysical Research 99 (B9), 17,805–17,825, doi: 10.1029/94JB00652.

Farrand, W. H., Lane, M. D., Edwards, B. R., Yingst, R. A., 2011. Spectral evidence of volcanic cryptodomes on the northern plains of Mars. Icarus, 211(1), 139-156, doi: 10.1016/j.icarus.2010.09.006.

Fassett, C. I., Levy, J. S., Head, J. W., Dickson, J. L., 2014. Long-lived Glaciation in the Northern Mid-Latitudes of Mars: New Constraints on Timing, Lunar Planet. Sci. 45, LPI Contribution No. 1777, abstract 1494.

Fergason, R.L., Christensen, P.R., Kieffer, H.H., 2006. High-resolution thermal inertia derivation from THEMIS: Thermal model and applications. J. Geophys. Res. 111, E12004, 22 pp, doi:10.1029/2006JE002735.

Fink, J.H. and Griffiths, R.W., 1998. Morphology, eruption rates, and rheology of lava domes: Insights from laboratory models, Journal of Geophysical Research-Solid Earth, 103 (B1) pp. 527–545, doi: 10.1029/97JB02838.

Greeley, R., and Guest, J.E., 1987. Geological Map of the Eastern Equatorial Region of Mars I-1802-B. U.S. Geological Survey, Flagstaff, AZ, USA.

Greeley, R., and Spudis, P. D., 1981. Volcanism on Mars, Rev. Geophys., 19(1), 13-41.

Grott M., Baratoux, D., Hauber, E., Sautter, V., Mustard, J., Gasnault, O., Ruff, S.W., Karato, S.-I., Debaille, V., Knapmeyer, M., Sohl, F., Van Hoolst, T., Breuer, D., Morschhauser, A., Toplis, M.J., 2013. Long-Term Evolution of the Martian Crust-Mantle System, Space Sci Rev, doi:10.1007/s11214-012-9948-3.

Gwinner, K., Scholten, F., Preusker, F., Elgner, S., Roatsch, T., Spiegel, M., Schmidt, R., Oberst, J., Jaumann, R., Heipke, C., 2010. Topography of Mars from global mapping by HRSC high-resolution digital terrain 2 models and orthoimages: Characteristics and performance, Earth Planet. Sci. Lett., 294, 506–519, doi:10.1016/j.epsl.2009.11.007.

Hartmann, W.K., and Neukum, G., 2001. Cratering chronology and the evolution of Mars, Space Science Reviews 96 (1/4), 165–194, doi: 10.1023/A:1011945222010.

Hartmann, W.K., and Werner, S. C., 2010. Martian Cratering 10. Progress in use of crater counts to interpret geological processes: Examples from two debris aprons, Earth Planet. Sci. Lett. 294, 230-237, doi: 10.1016/j.epsl.2009.10.001.

Hauber, E., van Gasselt, S., Chapman, M. G., Neukum, G., 2008. Geomorphic evidence for former lobate debris aprons at low latitudes on Mars: Indicators of the Martian paleoclimate, Journal of Geophysical Research, 113(E2), E02007, doi:10.1029/2007JE002897

Hauber, E., Bleacher, J., Gwinner, K., Williams, D., Greeley, R., 2009. The topography and morphology of low shields and associated landforms of plains volcanism in the Tharsis region of Mars, J. Volcanol. Geotherm. Res., 185, 69-95, doi: 10.1016/j.jvolgeores.2009.04.015.

Hauber, E., Brož, P., Jagert, F., Jodłowski, P., Platz, T., 2011. Very recent and widespread basaltic volcanism on Mars, Geophys. Res. Lett. 28, L10201. doi:10.1029/2011GL047310.

Head, J. W., Marchant, D. R., Dickson, J. L., Kress, A. M., Baker, D. M., 2010. Northern mid-latitude glaciation in the Late Amazonian period of Mars: Criteria for the recognition of debris-covered glacier and valley glacier landsystem deposits, Earth and Planetary Science Letters, 294(3-4), 306–320, doi:10.1016/j.epsl.2009.06.041.

Holt, J. W., Safaeinili, A., Plaut, J. J., Head, J. W., Phillips, R. J., Seu, R., Kempf, S. D., Choudhary, P., Young, D. A., Putzig, N. E., 2008. Radar sounding evidence for buried glaciers in the southern mid-latitudes of Mars, Science, 322(5905), 1235–1238.

Ivanov, B.A., 2001. Mars/Moon Cratering Rate Ratio Estimates, Space Sci. Rev. 96 (1/4), 87–104 doi: 10.1023/A:1011941121102.

Irwin III, R.P., Howard, A.D., Maxwell, T.A., 2004. Geomorphology of Ma'adim Vallis, Mars, and associated paleolake basins. J. Geophys. Res. 109 (E12), E12009. doi: 10.1029/2004JE002287.

Jankowski, D. G., and Squyres, S. W., 1992. The topography of impact craters in 'softened' terrain on Mars. Icarus , 100, 26–39, doi: 10.1016/0019-1035(92)90015-Y.

Jaumann, R., et al., 2007. The high-resolution stereo camera (HRSC) experiment on Mars Express: instrument aspects and experiment conduct from interplanetary cruise through the nominal mission, Planet. Space Sci. 55, 928–952, doi: 10.1016/j.pss.2006.12.003.

Kneissl, T., van Gasselt, S., Neukum, G., 2011. Map-projection-independent crater size-frequency determination in GIS environments – new software tool for ArcGIS, Planet. Space Sci., 59, 1243–1254, doi: 10.1016/j.pss.2010.03.015.

Kress, A. M., and Head, J. W., 2008. Ring-mold craters in lineated valley fill and lobate debris aprons on Mars: Evidence for subsurface glacial ice, Geophys. Res. Lett. 35, L23206, doi: 10.1029/2008GL035501.

Levy, J., Head, J. W., Marchant, D. R., 2010. Concentric crater fill in the northern mid-latitudes of Mars: Formation processes and relationships to similar landforms of glacial origin, Icarus, 209(2), 390–404, doi:10.1016/j.icarus.2010.03.036.

Malin, M. C., et al., 2007. Context camera investigation on board the Mars Reconnaissance Orbiter, J. Geophys.Res.112, E05S04, doi: 10.1029/2006JE002808.

Mangold, N., 2003. Geomorphic analysis of lobate debris aprons on Mars at Mars Orbiter Camera scale: Evidence for ice sublimation initiated by fractures, J. Geophys. Res. 108(E4), 8021, doi: 10.1029/2002JE001885.

Mercier, E., Outtani, F., De Lamotte, D. F., 1997. Late-stage evolution of fault-propagation folds: principles and example Journal of Structural Geology, 19, 185-193, doi: 10.1016/S0191-8141(96)00081-8.

McEwen, A. S., et al., 2007. Mars Reconnaissance Orbiter's High Resolution Imaging Science Experiment (HiRISE), J. Geophys. Res. 112, E05S02, doi: 10.1029/2005JE002605.

Meresse, S., Costard, F., Mangold, N., Masson, P., Neukum, G., the HRSC Co-I Team, 2008. Formation and evolution of the chaotic terrains by subsidence and magmatism: Hydraotes Chaos, Mars, Icarus 194, 487–500, doi: 10.1016/j.icarus.2007.10.023.

Meslin, P.-Y., et al., 2013. Soil diversity and hydration as observed by ChemCam at Gale Crater, Mars, Science, 341(6153), doi:10.1126/science.1238670.

Michael, G.G., and Neukum, G., 2010. Planetary surface dating from crater size-frequency distribution measurements: Partial resurfacing events and statistical age uncertainty, Earth Planet. Sci. Lett. 294, 223–229, doi:10.1016/j.epsl.2009.12.041.

Michael, G.G., Platz, T., Kneissl, T., Schmedemann, N., 2012. Planetary surface dating from crater size-frequency distribution measurements: a quantitative test of spatial randomness, Icarus 218, 169-177, doi:10.1016/j.icarus.2011.11.033.

Morgan, G. A., Head, J. W., Marchant, D. R., 2009. Lineated valley fill (LVF) and lobate debris aprons (LDA) in the Deuteronilus Mensae northern dichotomy boundary region, Mars: Constraints on the extent, age and episodicity of Amazonian glacial events, Icarus 202, 22-38, doi: 10.1016/j.icarus.2009.02.017.

Mustard, J.F., Cooper, C.D., Rifkin, M.K., 2001. Evidence for recent climate change on Mars from the identification of youthful near-surface ground ice. Nature 412, 411–414, doi: 10.1038/35086515.

Neish, C. D., Lorenz, R. D., Kirk, R. L., 2008. Radar topography of domes on planetary surfaces, Icarus 196 552–564, doi:10.1016/j.icarus.2008.03.013.

Ody, A., Poulet, F., Langevin, Y., Bibring, J.-P., Bellucci, G., Altieri, F., Gondet, B., Vincendon, M., Carter, J., Manaud, N., 2012. Global maps of anhydrous minerals at the surface of Mars from OMEGA/MEx, J. Geophys. Res. Planets, 117, doi:10.1029/2012JE004117.

Parsons, R. A., and Holt, J. W., 2014. Determining the Age and Physical Properties of Martian Lobate Debris Aprons Using High-Resolution Topography, SHARAD Observations, and Numerical Ice Flow Modeling: A Case Study at Euripus Mons, Lunar Planet. Sci. 45, LPI Contribution No. 1777, abstract 1484.

Platz, T., and Michael, G.G., 2011. Eruption history of the Elysium Volcanic Province, Mars. Earth and Planetary Science Letters 312, 140-151, doi:10.1016/j.epsl.2011.10.001.

Platz, T., Cronin, S.J., Procter, J.N., Neall, V.E., Foley, S.F., 2012. Non-explosive, dome-forming eruptions at Mt. Taranaki, New Zealand. Geomorphology (Special Issue: Volcano Geomorphology: landforms, processes and hazards) 136, 15-30. (doi:10.1016/j.geomorph.2011.06.016).

Plaut, J. J., Safaeinili, A., Holt, J. W., Phillips, R. J., Head, J. W., Seu, R., Putzig, N. E., Frigeri, A., 2009. Radar evidence for ice in lobate debris aprons in the mid-northern latitudes of Mars, Geophysical Research Letters, 36(2), L02203, doi:10.1029/2008GL036379.

Rampey, M. L., Milam, K. A., McSween, H. Y. Jr., Moersch, J. E., Christensen, P. R., 2007. Identity and emplacement of domical structures in the western Arcadia Planitia, Mars, Journal of Geophysical Research, vol. 112, E06011, doi:10.1029/2006JE002750.

Robbins, S. J., Di Achille, G., B. Hynek, M., 2011. The volcanic history of Mars: High-resolution crater-based studies of the calderas of 20 volcanoes, Icarus 211, 1179–1203, doi:10.1016/j.icarus.2010.11.012.

Rogers, N., and Hawkesworth, C., 2000. Composition of magmas. In: Sigurdsson, H., Houghton, B., McNutt, S.R., Rymer, H., Stix, J. (Eds.), Encyclopedia of Volcanoes. Academic Press, pp. 307–320.

Sautter, V. et al., 2014. Igneous mineralogy at Bradbury Rise: The first ChemCam campaign at Gale crater, Journal of Geophysical Research: Planets, Volume 119, Issue 1, pages 30–46,, doi :10.1002/2013JE004472

Scott, D.H., and Tanaka, K.L., 1986. Geologic map of the western equatorial region of Mars. USGS Misc. Invest. Series Map I-1802-A.Sheridan, M.F., and K.H. Wohletz (1983), Hydrovolcanism: basic considerations and review, J. Volcanol. Geotherm. Res., 17, 1-29, doi: 10.1016/0377-0273(83)90060-4.

Scholten, F., Gwinner, K., Roatsch, T., Matz, K.-D., Wählisch, M., Giese, B., Oberst, J., Jaumann, R., Neukum, G., the HRSC Co-Investigator Team, 2005. Mars Express HRSC Data Processing - Methods and Operational Aspects, PE&RS, 71, 1143–1152.

Schultz, R.A., 200. Localization of bedding plane slip and backthrust faults above blind thrust faults: Keys to wrinkle ridge structure Journal of Geophysical Research 105, 12035-12052, doi: 10.1029/1999JE001212.

Skok, J.R., Mustard, J.F., Ehlmann, B.L., Milliken, R.E., Murchie, S.L., 2010. Silica deposits in the Nili Patera caldera on the Syrtis Major volcanic complex on Mars, Nat. Geosci., 3 (2010), 838–841, doi:10.1038/ngeo990.

Smith, D.E. et al., 2001. Mars Orbiter Laser Altimeter: Experiment summary after the first year of global mapping of Mars. J. Geophys. Res. 106 (E10), 23689–23722, doi: 10.1029/2000JE001364.

Souness, C., and Hubbard, B., 2012. Mid-latitude glaciation on Mars, Progress in Physical Geography 36(2), doi: 10.1177/0309133312436570.

Squyres, S.W., 1978. Martian fretted terrain: flow of erosional debris. Icarus, 34, 600-613, doi: 10.1016/0019-1035(78)90048-9.

Squyres, S.W., and Carr, M. H., 1986. Geomorphic evidence for the distribution of ground ice on Mars, Science 231(4735):249-52, doi: 10.1126/science.231.4735.249.

Stolper, E.M. et al., 2013. The Petrochemistry of Jake_M: A Martian Mugearite, Science 341, doi: 10.1126/science.1239463.

Tanaka, K.L., Skinner, J.A., Jr., Dohm, J.M., Irwin, R.P., III, Kolb, E.J., Fortezzo, C.M., Platz, T., Michael, G.G., Hare, T.M, 2104. Geologic Map of Mars. U.S. Geological Survey Scientific Investigations Map SIM 3292, 1:20,000,000.

Vaucher, J., Baratoux, D., Mangold, N., Pinet, P., Kurita, K., Grégoire, M., 2009. The volcanic history of central Elysium Planitia: Implications for Martian magmatism, Icarus, 204, 418–442, doi:10.1016/j.icarus.2009.06.032.

Washburn, A.L., 1956. Classification of patterned ground and review of suggested origins, Geol. Soc. Amer. Bull., 67(7), 823-865.

Wendt, L., Bishop, J., Neukum, G., 2013. Knob fields in the Terra Cimmeria/Terra Sirenum region of Mars: Stratigraphy, mineralogy and morphology, Icarus 225, 200–215, doi: 10.1016/j.icarus.2013.03.020.

Werner, S.C., 2009. The global martian volcanic evolutionary history, Icarus 201, 44–68, doi: 10.1016/j.icarus.2008.12.019.

Williams, D. A., Greeley, R., Fergason, R. L., Kuzmin, R., McCord, T. B., Combe, J.-P., Head III, J. W., Xiao, L., Manfredi, L., Poulet, F., Pinet, P., Baratoux, D., Plaut, J. J., Raitala, J., Neukum, G., the HRSC Co-Investigator Team, 2009. The Circum-Hellas Volcanic Province, Mars: Overview, Planetary and Space Science 57, 895–916, doi: 10.1016/j.pss.2008.08.010.

Wilson, L. and Head III, J.W., 2002. Tharsis-radial graben systems as the surface manifestation of plume-related dike intrusion complexes: Models and implications. J. Geophys. Res. 107, doi: 10.1029/2001JE001593.

Wray, J.J., Hansen, S. T., Dufek, J., Swayze, G. A., Murchie, S. L., Seelos, F. P., Skok, J. R., Irwin, R. P., Ghiorso, M. S., 2013. Prolonged magmatic activity on Mars inferred from the detection of felsic rocks, Nature Geoscience 6, 1013–1017, doi: 10.1038/NGEO1994.

Xiao, L., Huang, J., Christensen, P. R., Greeley, R., Williams, D. A., Zhao, J., He, Q., 2012, Ancient volcanism and its implication for thermal evolution of Mars, Earth Planet. Sci. Lett., 323–324, 9–18, doi:10.1016/j. epsl.2012.01.027.

Zuber, M. T., Smith, D. E., Solomon, S. C., Muhleman, D. O., Head, J. W., Garvin, J. B., Abshire, J. B., Bufton, J. L., 1992. The Mars Observer Laser Altimeter investigation, J. Geophys. Res., 97, 7781–7797, doi:10.1029/92JE00341.